Acta Crystallographica Section D
Biological Crystallography
ISSN 0907-4449
Editors: **E. N. Baker and Z. Dauter**

Structural reorganization of the bacterial cell-division protein FtsZ from *Staphylococcus aureus*

Takashi Matsui, Junji Yamane, Nobuyuki Mogi, Hiroto Yamaguchi, Hiroshi Takemoto, Min Yao and Isao Tanaka

Acta Cryst. (2012). D**68**, 1175–1188

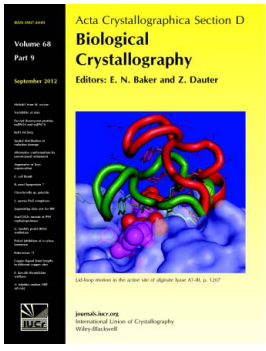

Acta Crystallographica Section D: Biological Crystallography welcomes the submission of papers covering any aspect of structural biology, with a particular emphasis on the structures of biological macromolecules and the methods used to determine them. Reports on new protein structures are particularly encouraged, as are structure–function papers that could include crystallographic binding studies, or structural analysis of mutants or other modified forms of a known protein structure. The key criterion is that such papers should present new insights into biology, chemistry or structure. Papers on crystallographic methods should be oriented towards biological crystallography, and may include new approaches to any aspect of structure determination or analysis. Papers on the crystallization of biological molecules will be accepted providing that these focus on new methods or other features that are of general importance or applicability.

Acta Crystallographica Section D
Biological Crystallography
ISSN 0907-4449

Structural reorganization of the bacterial cell-division protein FtsZ from *Staphylococcus aureus*

Takashi Matsui,[a]‡ Junji Yamane,[b,c]‡ Nobuyuki Mogi,[b] Hiroto Yamaguchi,[c] Hiroshi Takemoto,[c] Min Yao[a,b] and Isao Tanaka[a,b]*

[a]Faculty of Advanced Life Science, Hokkaido University, Sapporo, Hokkaido 060-0810, Japan, [b]Graduate School of Life Science, Hokkaido University, Sapporo, Hokkaido 060-0810, Japan, and [c]Shionogi Innovation Center for Drug Discovery, Discovery Research Laboratories, Shionogi & Co. Ltd, Sapporo, Hokkaido 001-0021, Japan

‡ TM and JY contributed equally to this work.

Correspondence e-mail: tanaka@castor.sci.hokudai.ac.jp

Received 26 April 2012
Accepted 18 May 2012

PDB References: *Sa*FtsZf-GDP, 3vo8; apo *Sa*FtsZt (SeMet), 3vo9; apo *Sa*FtsZt, 3vpa; *Sa*FtsZt-GDP, 3voa; *Sa*FtsZt-GDP, PC190723 complex, 3vob.

FtsZ is a key molecule in bacterial cell division. In the presence of GTP, it polymerizes into tubulin-like protofilaments by head-to-tail association. Protofilaments of FtsZ seem to adopt a straight or a curved conformation in relation to the bound nucleotide. However, although several bacterial and archaeal FtsZ structures have been determined, all of the structures reported previously are considered to have a curved conformation. In this study, structures of FtsZ from *Staphylococcus aureus* (*Sa*FtsZ) were determined in apo, GDP-bound and inhibitor-complex forms and it was found that *Sa*FtsZ undergoes marked conformational changes. The accumulated evidence suggests that the GDP-bound structure has the features of the straight form. The structural change between the curved and straight forms shows intriguing similarity to the eukaryotic cytoskeletal protein tubulin. Furthermore, the structure of the apo form showed an unexpectedly large conformational change in the core region. FtsZ has also been recognized as a novel target for antibacterial drugs. The structure of the complex with the inhibitor PC190723, which has potent and selective antistaphylococcal activity, indicated that the inhibitor binds at the cleft between the two subdomains.

1. Introduction

FtsZ is a prokaryotic homologue of eukaryotic cytoskeletal tubulin and is a key molecule in bacterial cell division (Adams & Errington, 2009; Margolin, 2005). During bacterial cell division, FtsZ polymerizes into tubulin-like protofilaments by head-to-tail association (Oliva *et al.*, 2004). Subsequently, it recruits many accessory proteins that are also essential for cell division (Adams & Errington, 2009). In *Escherichia coli* (*E. coli*), these accessory proteins bundle the filaments and anchor them to the cytoplasmic membrane (Pichoff & Lutkenhaus, 2002); consequently, a contractile ring-like structure known as the Z-ring is formed at the midpoint of the cell (Margolin, 2005).

Structurally, FtsZ consists of an N-terminal enzymatic domain and a long C-terminal extension of about 80 residues. The enzymatic domain is composed of two globular subdomains (N- and C-terminal subdomains) separated by a central core helix (H7 helix). There is a nucleotide-binding pocket in the N-terminal subdomain (residues 12–171). The C-terminal subdomain is likely to be a GTPase-activating subdomain (residues 223–310). At the tip of the long C-terminal extension is the functional site that recognizes the accessory proteins (Mosyak *et al.*, 2000; Yan *et al.*, 2000).

FtsZ is a self-activating GTPase (de Boer *et al.*, 1992; RayChaudhuri & Park, 1992). For polymerization, the T7 loop in the 'upper' subunit is inserted into the nucleotide-binding pocket of the 'lower' subunit (Löwe & Amos, 1999). Mutation

of Asn207, Asp209 and Asp212 in the T7 loop of *E. coli* FtsZ (*Ec*FtsZ) severely affects GTP hydrolysis (Scheffers *et al.*, 2002). These results suggested that the catalytic residues in the T7 loop are located near the γ-phosphate of GTP and thus GTP hydrolysis proceeds. GTPase activity therefore depends on FtsZ polymerization (Oliva *et al.*, 2004; Scheffers *et al.*, 2002).

Protofilaments of FtsZ seem to adopt a straight or a curved conformation in relation to the bound nucleotide (Lu *et al.*, 2000; Huecas & Andreu, 2003). Previous investigations have suggested that FtsZ acts as a nucleotide-regulated molecular switch in the assembly/disassembly cycle of cell division (Martín-Galiano *et al.*, 2010; Chen & Erickson, 2011). *Ec*FtsZ with GTP may switch from the curved to the straight conformation (Chen & Erickson, 2011). However, although several structures of bacterial and archaeal FtsZs have been determined (Löwe & Amos, 1998; Leung *et al.*, 2004), they are all very similar irrespective of the bound nucleotide (Oliva *et al.*, 2007). The slight differences observed to date seem to be related to interspecies differences. The crystal structure of *Methanococcus jannaschii* FtsZ (*Mj*FtsZ) formed a tilted dimer (Oliva *et al.*, 2004) and the relative disposition of the two monomers seemed to be related to the curved structures of tubulin (Buey *et al.*, 2006). Thus, all FtsZ structures analyzed previously were considered to be in the curved conformation (Oliva *et al.*, 2007) and the straight conformation has only been visualized at low resolution (Löwe & Amos, 1999). The latter conformation is necessary to understand the molecular mechanism of FtsZ; *i.e.* how it polymerizes and hydrolyzes GTP at the molecular level.

FtsZ is essential for bacterial cell division in almost all prokaryotes and is absent in eukaryotes, except in the chloroplasts of plants and in the mitochondria of some primitive organisms. Therefore, FtsZ has been recognized as a novel target for antibacterial drugs (Lock & Harry, 2008). Several compounds have been shown to block bacterial cell division and/or to inhibit the function of FtsZ *in vitro* (Ohashi *et al.*, 1999; Domadia *et al.*, 2007; Stokes *et al.*, 2005; Läppchen *et al.*, 2008). In particular, the inhibitor 2,6-difluoro-3-[(6-chlorothiazolo[5,4-*b*]pyridine)-2-ylmethoxy]benzamide (PC190723) has been reported to have a potent and selective anti-staphylococcal activity (Andreu *et al.*, 2010; Haydon *et al.*, 2008). PC190723 binds to FtsZ with GTP (Andreu *et al.*, 2010) and is therefore suggested to interact with straight FtsZ.

In the present study, we investigated the structures of FtsZ from *Staphylococcus aureus* (*Sa*FtsZ) in apo, GDP-bound and PC190723-complex forms, and showed that FtsZ undergoes distinct conformational changes. Here, we discuss these structural features and relate them to the crucial functions of FtsZ.

2. Materials and methods

2.1. Protein expression and purification of *Sa*FtsZ

Full-length FtsZ from *S. aureus* Mu50 (*Sa*FtsZf) and its enzymatic domain (residues 12–316; *Sa*FtsZt) were amplified by PCR and cloned into the *Nde*I/*Xho*I sites of the pET-28b(+) vector (Merck KGaA). The primers were designed based on the DNA sequence in GenBank (accession No. 15924176). *Sa*FtsZf and *Sa*FtsZt were expressed and purified using the same procedure. The proteins were overexpressed in *E. coli* strain BL21 (DE3) as recombinant fusion proteins with an N-terminal hexahistidine tag and TEV protease recognition sequence. Cells were grown at 310 K in Luria broth with 25 mg l^{-1} kanamycin until the optical density reached 0.6. After the addition of 0.25 m*M* isopropyl β-D-1-thiogalactopyranoside, growth was continued for 3 h at 310 K. The cells were harvested and resuspended in lysis buffer [50 m*M* Tris–HCl pH 8.0, 300 m*M* NaCl, 10%(*v*/*v*) glycerol, 0.5 mg ml^{-1} lysozyme, 0.1 mg ml^{-1} DNase I]. The cell lysate was sonicated and then centrifuged at 40 000*g* for 30 min at 283 K. The supernatant was loaded onto a 5 ml HisTrap HP column (GE Healthcare). After washing the column with buffer *A* [50 m*M* Tris–HCl pH 8.0, 300 m*M* NaCl, 10%(*v*/*v*) glycerol], the fusion protein was eluted using a stepwise increasing imidazole concentration: 50, 250 and 500 m*M*. Fractions containing the desired protein were incubated with TEV protease (Merck KGaA) and dialyzed against buffer *A* at 277 K; the mixtures were then loaded onto a 5 ml HisTrap HP column. The flow-through fraction was collected and further purified by gel filtration on HiLoad 16/60 Superdex 200 (GE Healthcare) pre-equilibrated with buffer *B* (50 m*M* Tris–HCl pH 8.0, 300 m*M* NaCl). After gel filtration, *Sa*FtsZ was diluted fivefold with buffer *C* (50 m*M* Tris–HCl pH 8.0) and purified on a 1 ml Resource Q column (GE Healthcare) using a linear gradient of buffer *C* to buffer *D* (50 m*M* Tris–HCl pH 8.0, 1 *M* NaCl). The purified protein was exchanged into buffer *B* using a Vivaspin 20 10k ultrafiltration device (GE Healthcare). *Sa*FtsZf and *Sa*FtsZt were concentrated to 10.0 and 5.0 mg ml^{-1}, respectively, using Vivaspin 20 10k ultrafiltration devices (GE Healthcare).

SeMet-labelled *Sa*FtsZt [*Sa*FtsZt (SeMet)] was overexpressed in *E. coli* strain B834 (DE3). Cells were grown at 310 K in M9 medium containing 1 m*M* $MgSO_4$, 0.1 m*M* $CaCl_2$, 1× BME vitamins solution (Sigma–Aldrich), 0.4% glucose, 25 mg l^{-1} selenomethionine, 14 mg l^{-1} each of 19 amino acids and 50 mg l^{-1} kanamycin until the optical density reached 0.3. After the addition of 0.25 m*M* isopropyl β-D-1-thiogalactopyranoside, growth was continued for 11 h at 310 K. Purification of *Sa*FtsZt (SeMet) was performed as described above.

2.2. *Sa*FtsZ mutagenesis

Mutant *Sa*FtsZ was prepared using a Stratagene QuikChange mutagenesis kit (Agilent Technologies) with *Sa*FtsZf expression vector as a template. Asn208 was substituted by Ala (to give *Sa*FtsZf N208A). The DNA sequence was confirmed using an ABI 310 Genetic Analyzer (Applied Biosystems). The mutant protein was prepared as described above.

2.3. Crystallization and structure determination

All crystals were obtained using the conditions shown in Table 1 and appeared after a few weeks at 293 K. (Although

Table 1
Summary of crystallization conditions, data-collection and refinement statistics.

Values in parentheses are for the highest resolution shell.

	*Sa*FtsZf-GDP	*Sa*FtsZt-GDP†	Apo *Sa*FtsZt (SeMet)†	Apo *Sa*FtsZt†	PC190723 complex
PDB code	3vo8	3voa	3vo9	3vpa	3vob
Sample condition	Native *Sa*FtsZf	Native *Sa*FtsZt	SeMet *Sa*FtsZt	Native *Sa*FtsZt	Native *Sa*FtsZt
Crystallization conditions	0.2 *M* lithium sulfate, 0.1 *M* Tris–HCl pH 8.5, 30%(*w*/*v*) PEG 4000	0.2 *M* lithium sulfate, 0.1 *M* Tris–HCl pH 8.5, 25%(*w*/*v*) PEG 5000 MME, 10%(*v*/*v*) ethylene glycol	1.0 *M* lithium chloride, 0.1 *M* sodium acetate, 30%(*w*/*v*) PEG 6000, 0.34 *M* sodium malonate pH 7.0	1.0 *M* lithium chloride, 0.1 *M* sodium acetate, 30%(*w*/*v*) PEG 6000, 0.34 *M* sodium malonate pH 7.0	0.2 *M* lithium sulfate, 0.1 *M* Tris–HCl pH 8.5, 25%(*w*/*v*) PEG 5000 MME, 10%(*v*/*v*) ethylene glycol
Inhibitor	—	—	—	—	0.5 m*M* PC190723, 10%(*v*/*v*) 1-methyl-2-pyrrolidone
Cryoprotectant	20%(*v*/*v*) glycerol	—	—	—	—
Data collection					
Beamline	SPring-8 BL41XU	In-house	PF BL5A	Spring-8 BL41XU	In-house
Wavelength (Å)	1.0000	1.54	0.9791	1.0000	1.54
Space group	*P*1	*C*2	$P2_12_12_1$	$P2_12_12_1$	*C*2
Unit-cell parameters (Å, °)	*a* = 44.0, *b* = 44.1, *c* = 86.0, α = 96.9, β = 103.6, γ = 108.0	*a* = 72.8, *b* = 49.6, *c* = 88.4, β = 111.6	*a* = 72.9, *b* = 80.7, *c* = 225.3	*a* = 73.5, *b* = 81.1, *c* = 225.5	*a* = 72,1, *b* = 50.5, *c* = 88.3, β = 111.0
Resolution range (Å)	50.0–2.25 (2.31–2.25)	50.0–1.73 (1.78–1.73)	50.0–2.70 (2.80–2.70)	50.0–2.50 (2.59–2.50)	50.0–2.70 (2.80–2.70)
Completeness (%)	97.7 (91.3)	95.4 (90.3)	99.6 (100)	99.3 (100)	99.8 (99.8)
$\langle I/\sigma(I)\rangle$ (%)	20.8 (4.1)	14.2 (4.5)	25.1 (5.2)	17.7 (3.2)	7.2 (3.9)
R_{merge}‡ (%)	8.3 (28.5)	5.0 (14.9)	12.3 (48.5)	11.7 (41.7)	11.5 (35.2)
Multiplicity	2.9 (2.5)	2.7 (2.4)	14.3 (14.3)	7.2 (7.3)	3.3 (3.1)
No. of observed reflections	77083	80661	523986	345385	27346
No. of unique reflections	26872	29352	36669	47728	8238
Refinement					
Resolution (Å)	35.54–2.25	19.99–1.73	31.76–2.71	35.49–2.50	32.35–2.70
Overall R_{work}§ (%)	18.8	18.8	22.7	21.0	19.5
Overall R_{free}¶ (%)	23.7	23.0	27.2	25.8	24.7
Total atoms	4553	2510	8529	8492	2289
No. of protein atoms	4395	2215	8452	8353	2193
No. of ligand atoms	56	28	—	—	51
No. of metal atoms	2	1	—	—	1
No. of solvent atoms	100	266	77	139	44
Average *B* factors (Å^2)					
Protein atoms	32.0	22.8	48.1	57.6	25.8
Ligand atoms	25.3	16.6	—	—	24.4
Metal atoms	34.3	20.6	—	—	40.5
Solvent atoms	30.7	30.3	39.5	47.2	21.5
R.m.s.d. from ideal					
Bond lengths (Å)	0.009	0.007	0.012	0.009	0.015
Bond angles (°)	1.155	1.147	1.246	1.256	1.388
Ramachandran plot					
Favoured region	596 [98.5%]	301 [98.7%]	1063 [96.0%]	1126 [99.0%]	292 [96.7%]
Allowed region	9 [1.5%]	4 [1.3%]	44 [4.0%]	8 [1.0%]	10 [3.3%]
Outlier region	0 [0%]	0 [0%]	0 [0%]	0 [0%]	0 [0%]

† Met−1 and His−2 derived from *Nde*I and Gly−3, the C-terminal residue of the TEV recognition site, are also included in the structure. ‡ $R_{merge} = \sum_{hkl}\sum_i |I_i(hkl) - \langle I(hkl)\rangle| / \sum_{hkl}\sum_i I_i(hkl)$, where $\langle I(hkl)\rangle$ is the mean intensity of symmetry-equivalent reflections. § $R_{work} = \sum_{hkl} ||F_{obs}| - |F_{calc}|| / \sum_{hkl} |F_{obs}|$, where F_{obs} and F_{calc} are observed and calculated structure-factor amplitudes, respectively. ¶ The R_{free} value was calculated as for R_{work} but using only an unrefined subset of reflection data.

we did not add GDP to the crystallization buffer, the *Sa*FtsZf and *Sa*FtsZt crystals contained GDP. Therefore, they are hereafter referred to as *Sa*FtsZf-GDP and *Sa*FtsZt-GDP, respectively.) To obtain *Sa*FtsZt-GDP crystals complexed with PC190723 (PC190723 complex), cocrystallization experiments were carried out using the microseeding technique. X-ray diffraction data for *Sa*FtsZf-GDP were collected on beamline BL41XU at SPring-8, Hyogo, Japan under cryogenic conditions at 100 K. The diffraction data were processed and scaled with the *HKL*-2000 program package (Otwinowski & Minor, 1997). Molecular replacement was performed for *Sa*FtsZf-GDP with *MOLREP* in the *CCP*4 suite (Vagin & Teplyakov, 2010; Winn *et al.*, 2011) using PDB entry 2vxy (*Bacillus subtilis* FtsZ; *Bs*FtsZ; Haydon *et al.*, 2008) as the search model. The structure was rebuilt using the automatic refinement program *LAFIRE* (Yao *et al.*, 2006; Zhou *et al.*, 2006) running with *CNS* (Brünger *et al.*, 1998), modified manually with *Coot* (Emsley & Cowtan, 2004) and refined with *PHENIX* (Adams *et al.*, 2010).

Single-wavelength anomalous diffraction data were collected from a crystal of apo *Sa*FtsZt (SeMet) on beamline BL5A at Photon Factory, Tsukuba, Japan under cryogenic conditions at 100 K. A wavelength of 0.97910 Å was used for data collection based on the fluorescence spectrum of the Se *K* absorption edge (Rice *et al.*, 2000). The diffraction data for apo *Sa*FtsZt (SeMet) were processed and scaled using the *HKL*-2000 program package. Se sites were determined with

SHLEXD (Sheldrick, 2008, 2010). The sites were refined and initial phases were calculated with *Phaser* in *PHENIX*. Phase improvement and automatic model building were performed using *RESOLVE* (Terwilliger, 2000) in *PHENIX*. The structure of apo *Sa*FtsZt (SeMet) was refined with *PHENIX* and manually modified with *Coot*. X-ray diffraction data for apo *Sa*FtsZt were collected on beamline BL41XU at SPring-8, Hyogo, Japan under cryogenic conditions at 100 K. The diffraction data for apo *Sa*FtsZt were processed and scaled with the *HKL*-2000 program package. Molecular replacement was performed for apo *Sa*FtsZt with *MOLREP* in the *CCP*4 suite using apo *Sa*FtsZt (SeMet) as the search model. The structure was modified manually with *Coot* and refined with *PHENIX*.

The diffraction data for *Sa*FtsZt-GDP and the complex of *Sa*FtsZt-GDP with PC190723 were collected under cryogenic conditions (100 K) using in-house X-ray diffraction equipment consisting of a Rigaku FR-E SuperBright microfocus rotating-anode X-ray generator with VariMax optics, an X-stream 2000 low-temperature system and an R-AXIS VII detector. These diffraction data were processed and scaled with the *HKL*-2000 program package. Molecular replacement was performed for *Sa*FtsZt-GDP with *MOLREP* in the *CCP*4 suite using PDB entry 2vxy (*Bs*FtsZ; Haydon *et al.*, 2008) as the search model. After phase determination, automatic restrained positional and isotropic *B*-factor refinement was performed using *ARP*/*wARP* (Langer *et al.*, 2008) with *REFMAC*5 (Murshudov *et al.*, 2011). The final step of refinement was carried out using *LAFIRE* (Yao *et al.*, 2006; Zhou *et al.*, 2006), *REFMAC*5 and *Coot*. Molecular replacement was performed for the PC190723 complex with *MOLREP* in the *CCP*4 suite using *Sa*FtsZf-GDP as the search model. The structure was modified manually with *Coot* and refined with *PHENIX*.

Data-collection and refinement statistics are summarized in Table 1. Structures were displayed using *PyMOL* (DeLano, 2002). The coordinates and structure factors of *Sa*FtsZf-GDP, apo *Sa*FtsZt (SeMet), apo *Sa*FtsZt, *Sa*FtsZt-GDP and the complex of *Sa*FtsZt-GDP with PC190723 have been deposited in the RCSB Protein Data Bank under accession codes 3vo8,

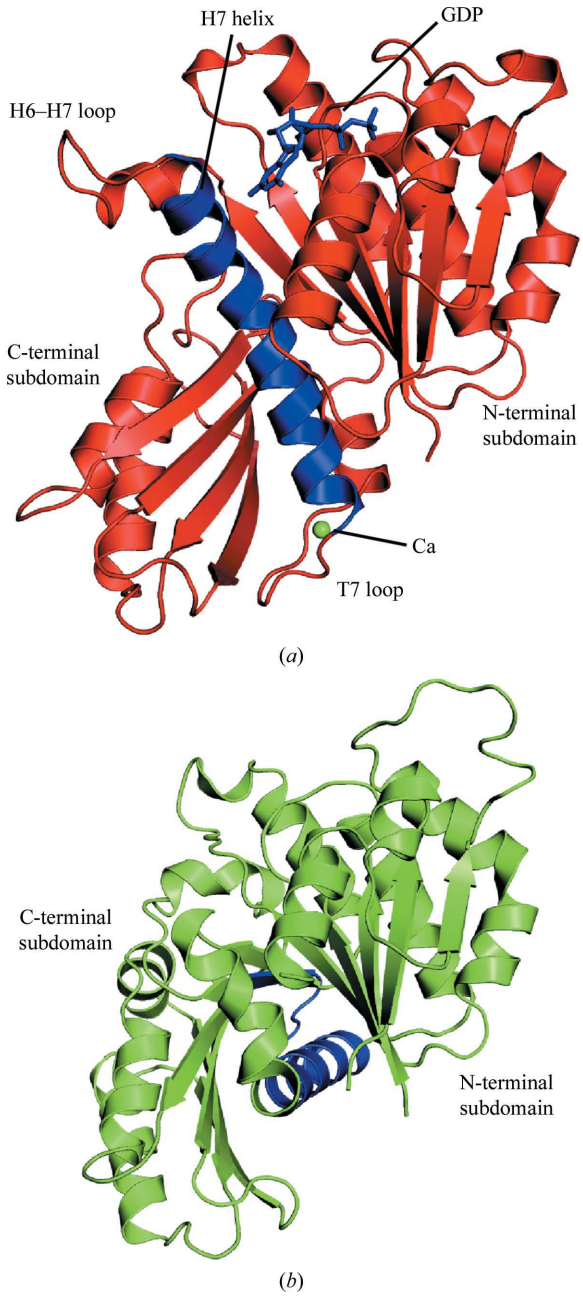

Figure 1
Structures of FtsZ. (*a*) The structure of GDP-form *Sa*FtsZ is shown in cartoon representation. The molecule is coloured red, except for the H7 helix (residues 179–202), which is shown in blue. GDP and the calcium ion are represented as blue sticks and a green sphere, respectively. (*b*) The structure of apo-form *Sa*FtsZt is coloured green. The structure of the central H7 helix has changed from that in (*a*) and the changes are highlighted in blue. (*c*) For comparison, the structure of *Bs*FtsZ with GDP (PDB entry 2rhl) is shown in cyan, except for the H7 helix (residues 179–202), which is shown in blue. GDP is represented as grey sticks. It is obvious that the H7 helix in (*a*) is downshifted from that in (*c*). All figures are shown after superposition of the N-terminal subdomain (residues 13–171).

3vo9, 3vpa, 3voa and 3vob, respectively. All figures of the apo-form conformation are illustrated using the coordinates of the native protein.

2.4. Hypothetical model building of the GTP-bound form

The conformation of the N-terminal subdomain of *Sa*FtsZ-GDP was very similar to that of GTP-bound *Mj*FtsZ. Based on the superimposed structures of *Sa*FtsZ-GDP and GTP-bound *Mj*FtsZ, a hypothetical model of GTP-bound *Sa*FtsZ was built by adding a γ-phosphate to *Sa*FtsZf-GDP at the end of the β-phosphate of GDP using *Coot* (Emsley & Cowtan, 2004). The model was refined using *REFMAC*5 (Murshudov *et al.*, 2011) to ensure that there was no steric hindrance between the hypothetical γ-phosphate and the other parts of the molecule apart from two water molecules. These water molecules were removed.

2.5. GTPase assay

The FtsZ GTPase assay was performed as described previously, with slight modifications (Haydon *et al.*, 2008). Exchange from GTP to GDP was monitored by determining the concentration of released phosphate using BIOMOL GREEN (BIOMOL Research Laboratories). GTP was added to 5 µ*M* *Sa*FtsZf in reaction buffer (50 m*M* MOPS pH 7.2, 5 m*M* $MgCl_2$, 200 m*M* KCl) at a final concentration of 100 µ*M* and incubated at 303 K for 1 h. To estimate the effect of calcium ions, the same experiments were performed in the presence of varying concentrations of $CaCl_2$ (0–10 m*M*).

2.6. Refolding of *Sa*FtsZ

As *Sa*FtsZf captures a calcium ion during culture of *E. coli* cells and the captured calcium ion is hardly removed, a calcium-ion-free form of *Sa*FtsZf was prepared by refolding chemically denatured *Sa*FtsZf. *Sa*FtsZf was purified by ion-exchange chromatography and denatured by 20-fold dilution with denaturing buffer [50 m*M* Tris–HCl pH 8.0, 300 m*M* NaCl, 10%(*v*/*v*) glycerol, 6 *M* urea]. After incubation at 277 K for 2 h, *Sa*FtsZf was refolded by dialysis against buffer *C*. Refolded *Sa*FtsZf was further purified by passage through a 1 ml Resource Q column with a linear gradient of buffer *C* to buffer *D*. The refolded sample was used for circular-dichroism measurements and sedimentation assay of *Sa*FtsZf.

2.7. Sedimentation assay

The sedimentation assay was performed using the procedure described previously, with slight modifications (Jaiswal & Panda, 2009). Samples containing 15 µ*M* protein were incubated for 30 min at 298 K in polymerization buffer (20 m*M* HEPES–KOH pH 7.5, 50 m*M* KCl, 1 m*M* $MgCl_2$) containing 1 m*M* GTP and various concentrations of $CaCl_2$ (0–7.5 m*M*). The polymers were collected by ultracentrifugation at 223 000*g* for 10 min at 298 K. The precipitates were resuspended in SDS–PAGE running buffer and subjected to SDS–PAGE.

2.8. Circular-dichroism measurements

Native and refolded *Sa*FtsZf were dialyzed against polymerization buffer. Samples of 0.2 mg ml^{-1} with or without 1 m*M* $CaCl_2$ were incubated at 298 K for 30 min in polymerization buffer with 1 m*M* GTP. The CD spectra of the samples were measured using a J-805 circular-dichroism spectrometer (JASCO Co.) in a quartz cell with an optical path length of 0.2 cm. The spectra were collected by taking the average of eight scans from 300 to 190 nm and were normalized to molar ellipticities. The helical content of the protein was estimated from the molar ellipticity at a wavelength of 222 nm (Price & Nairn, 2009).

3. Results

3.1. Structures of *Sa*FtsZ with GDP (*Sa*FtsZ-GDP)

We prepared crystals of full-length *Sa*FtsZ (residues 1–390; *Sa*FtsZf) and of the enzymatic domain (residues 12–316; *Sa*FtsZt). The structures of *Sa*FtsZf and *Sa*FtsZt were solved by the molecular-replacement method and were refined at resolutions of 2.25 and 1.73 Å, respectively (Table 1). The *Sa*FtsZf crystal had two molecules in the asymmetric unit; only residues 12–316 and 12–315 in molecules *A* and *B*, respectively, were visible. The two molecules superposed well, with a root-mean-square deviation (r.m.s.d.) of 0.19 Å for backbone C^{α} atoms. The *Sa*FtsZt crystal had one molecule in the asymmetric unit and residues 12–315 were observed in the electron-density map. Molecule *A* of *Sa*FtsZf superposed well with *Sa*FtsZt, with an r.m.s.d. of 0.39 Å for backbone C^{α} atoms (Supplementary Fig. S1[1]). Although GDP was not added to the crystallization conditions, the electron-density maps of the two crystals indicated the presence of GDP in the nucleotide-binding pocket of all molecules. Fig. 1(*a*) shows the structure of *Sa*FtsZf-GDP (molecule *A*); *Sa*FtsZf-GDP is composed of two globular subdomains separated by a long central H7 helix (residues 179–202) with two adjacent loops (the H6–H7 loop, residues 172–178, and the T7 loop, residues 203–209).

Although the two crystals belonged to different space groups (Table 1), they showed similar protofilament-like molecular associations (Fig. 2); two independent molecules of *Sa*FtsZf-GDP were aligned on the *a* and *b* axes in the unit cell of space group *P*1 and the *Sa*FtsZt-GDP molecules were aligned in the (**a** + **b**)/2 direction in the unit cell of space group *C*2. The repeating distances of the aligned molecules were approximately 44.0 Å (Table 1). As *Sa*FtsZf-GDP and *Sa*FtsZt-GDP have the same structural features, they are hereafter referred to as *Sa*FtsZ-GDP or the GDP form, unless otherwise indicated.

3.2. Structural comparison between *Sa*FtsZ and other FtsZs

A previous investigation suggested that the conformational differences observed in FtsZ crystals were related to inter-

[1] Supplementary material has been deposited in the IUCr electronic archive (Reference: MH5067). Services for accessing this material are described at the back of the journal.

species differences rather than interconversion between straight and curved conformations (Oliva *et al.*, 2007). That is, there were few conformational differences in the previous structures. In contrast to these previous results, the structures of *Sa*FtsZ showed clear differences from the structures reported to date. Figs. 3(*a*) and 3(*b*) show a structural comparison between the GDP-forms of *Sa*FtsZ and *Bs*FtsZ (PDB entry 2rhl, molecule *A*; Raymond *et al.*, 2009). Although the conformations of the N- and C-terminal subdomains in the *Sa*FtsZ were similar to those in *Bs*FtsZ (Table 2, Figs. 3*a* and 3*b*), a large difference was observed at the interface region around the H7 helix (Fig. 3*a*): the H7 helix was downshifted by about one helical pitch (Figs. 3*a*, 4*a*, 4*b* and 4*c*) and the following T7 loop with a coordinated calcium ion (as shown in §3.3) was inserted into the wider pocket of the 'lower' subunit (Fig. 4*a*). In addition, the H6–H7 loop moved away from the nucleotide-binding pocket (Fig. 4*b*).

To evaluate these conformational changes, we used the *DynDom* program, which determines protein domains, hinge axes and hinge-bending residues by comparing two conformations (Hayward & Berendsen, 1998). This program indicated that the C-terminal subdomain is rotated by about 25.2°. Residues 197–203 from the H7 helix to the T7 loop and residues 226–227 in the S7 strand of the C-terminal subdomain constitute the bending regions.

3.3. Coordination of divalent cation

The $F_o - F_c$ map showed a clear peak at coordination distances to Leu200, Val203, Asn208 and Leu209 in the T7 loop and to two water molecules (Fig. 5*a*). The distances between this residual peak and the carbonyl O atom of Leu200, the carbonyl O atom of Val203, Asn208 O^{δ}, the carbonyl O atom of Leu209 and two water molecules in *Sa*FtsZf-GDP were 2.31, 2.29, 2.40, 2.43, 2.45 and 2.46 Å, respectively (Supplementary Table S1). Although calcium ions were not added to the crystallization conditions, the observed distances and the coordination number were those of calcium coordination (Harding, 1999, 2001).

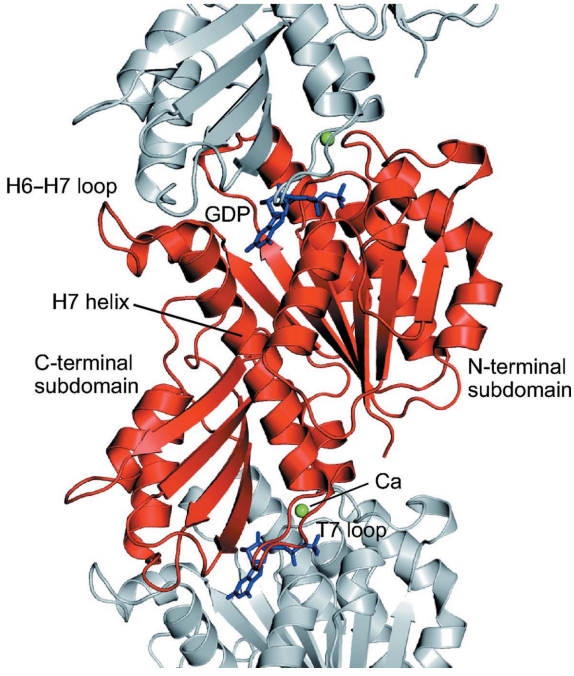

Figure 2
Crystal packing of *Sa*FtsZf-GDP (molecule *A*). An asymmetric molecule and symmetry-related molecules are coloured red and grey, respectively. GDP and calcium ions are represented as blue sticks and green spheres, respectively.

Table 2
R.m.s. conformational differences (Å) between *Sa*FtsZf-GDP and *Bs*FtsZ and between *Sa*FtsZf-GDP and the apo form.

The conformational differences between *Sa*FtsZf (molecule *A*) and *Bs*FtsZ (PDB entry 2rhl, molecule *A*) and between *Sa*FtsZf-GDP (molecule *A*) and the apo form (molecule *C*) were determined for C^{α} coordinates in the calculation region using *PyMOL* (DeLano, 2002). The N- and C-terminal subdomains are residues 13–171 and 223–310, respectively.

	Alignment region	
Calculation region	N-terminal subdomain	C-terminal subdomain
*Sa*FtsZf-GDP and *Bs*FtsZ		
N-terminal subdomain	0.68	14.60
C-terminal subdomain	7.52	1.93
*Sa*FtsZf-GDP and apo form		
N-terminal subdomain	4.31	17.59
C-terminal subdomain	7.85	2.15

Calcium ions are known to promote the assembly and bundling of protofilaments in *E. coli* (Yu & Margolin, 1997; Mukherjee & Lutkenhaus, 1999; Jaiswal & Panda, 2009; Marrington *et al.*, 2004). The calcium concentration in *E. coli* cells can reach millimolar levels under some conditions (Yu & Margolin, 1997; Holland *et al.*, 1999). Moreover, the calcium concentration during cell division in *E. coli* is almost 20-fold higher than that in nondividing cells (Chang *et al.*, 1986). A previous study suggested that millimolar concentrations of calcium ions promote the assembly and bundling of protofilaments in *E. coli* FtsZ, but do not polymerize *Mycobacterium tuberculosis* FtsZ (*Mt*FtsZ; Jaiswal & Panda, 2009). However, it was not clear whether calcium ions also contribute to the assembly of *Sa*FtsZ. To examine the effect of calcium ions on assembly, we performed a sedimentation assay with $CaCl_2$ (Fig. 5*b*). A small amount of *Sa*FtsZf was precipitated on incubation with neither calcium ions nor GTP. Although *Sa*FtsZf was precipitated with GTP, polymerization of *Sa*FtsZf with 1 m*M* GTP was promoted by calcium ions in a concentration-dependent manner.

Circular-dichroism (CD) measurements of *Sa*FtsZf with and without $CaCl_2$ showed that calcium ions induced small alterations in the secondary structure of FtsZ (Fig. 5*c*). These results showed that calcium ions contribute to the assembly of *Sa*FtsZ, as previously observed for *Ec*FtsZ (Yu & Margolin, 1997; Mukherjee & Lutkenhaus, 1999; Jaiswal & Panda, 2009; Marrington *et al.*, 2004).

To confirm that calcium ions also affect GTPase activity, we measured the GTPase activities of *Sa*FtsZf in the presence of varying concentrations of $CaCl_2$ (Fig. 5*d*). The results indicated that the GTPase activity of *Sa*FtsZf was suppressed by calcium ions in a concentration-dependent manner. *Sa*FtsZf

showed a complete loss of GTPase activity in the presence of 10 m*M* $CaCl_2$.

3.4. Structure of apo *Sa*FtsZt (apo form)

As calcium ions were shown to promote the polymerization of *Sa*FtsZ by inhibiting hydrolysis (Fig. 5), we attempted to determine the crystal structure of *Sa*FtsZt in the absence of calcium ions. *Sa*FtsZt crystals without calcium ions were obtained by adding 340 m*M* sodium malonate pH 7.0 as a chelating reagent. The crystal structures of apo *Sa*FtsZt (SeMet) and native apo *Sa*FtsZt were solved at resolutions of 2.71 and 2.50 Å by the single-wavelength anomalous diffraction method and the molecular-replacement method, respectively (Table 1, Fig. 1*b*, Supplementary Fig. S2). There were four molecules in the asymmetric unit of space group $P2_12_12_1$ and the electron-density map allowed us to build residues 12–315, with the exception of some disordered residues. The r.m.s.d. values of these molecules were less than 0.77 Å, except for in high-flexibility regions (Supplementary Fig. S3a and Table S2). The T3 loop (residues 66–75) and the S7–H9 loop (residues 231–236) have different conformations in the four asymmetric molecules and the H1–S2 loop (residues 31–37) and T5 loop (residues 136–146) were disordered, except for in molecule *C*. The conformations of the native and the SeMet protein were the same (r.m.s.d. of 0.42 Å; Supplementary Fig. S2). As neither GDP nor malonate ions were found in the crystals, we refer to these crystals as the apo form.

The overall structure of the apo form was very different from any of the previously determined FtsZ structures (Fig. 1, Table 2). The conformational changes were mainly in the interface region from the H6 helix to the H8 helix (in the GDP form). The residues from the H6 helix to Gln192 in the H7 helix of the GDP form formed a new kinked helix in the apo form (Fig. 4*d*). A new strand was also formed in the region from Asp199 of the H7 helix to Ser204 of the T7 loop in the GDP form. This new strand participates in both N- and C-terminal β-sheets. Thus, the secondary structure of the apo form was markedly changed from that of the GDP form (Figs. 4*e* and 4*f*). The conformational changes were accompanied by a change in the relative orientation between the two subdomains. The subdomain rotation from *Bs*FtsZ (36.0°) was larger than that of the GDP form from *Bs*FtsZ (25.2°). The *DynDom* program (Hayward & Berendsen, 1998) estimated that the hinge regions were residues 164–165 in the S6 strand, 192–199 in the H7 helix, and 197–224 from the H7 helix to the H8 helix in the GDP form.

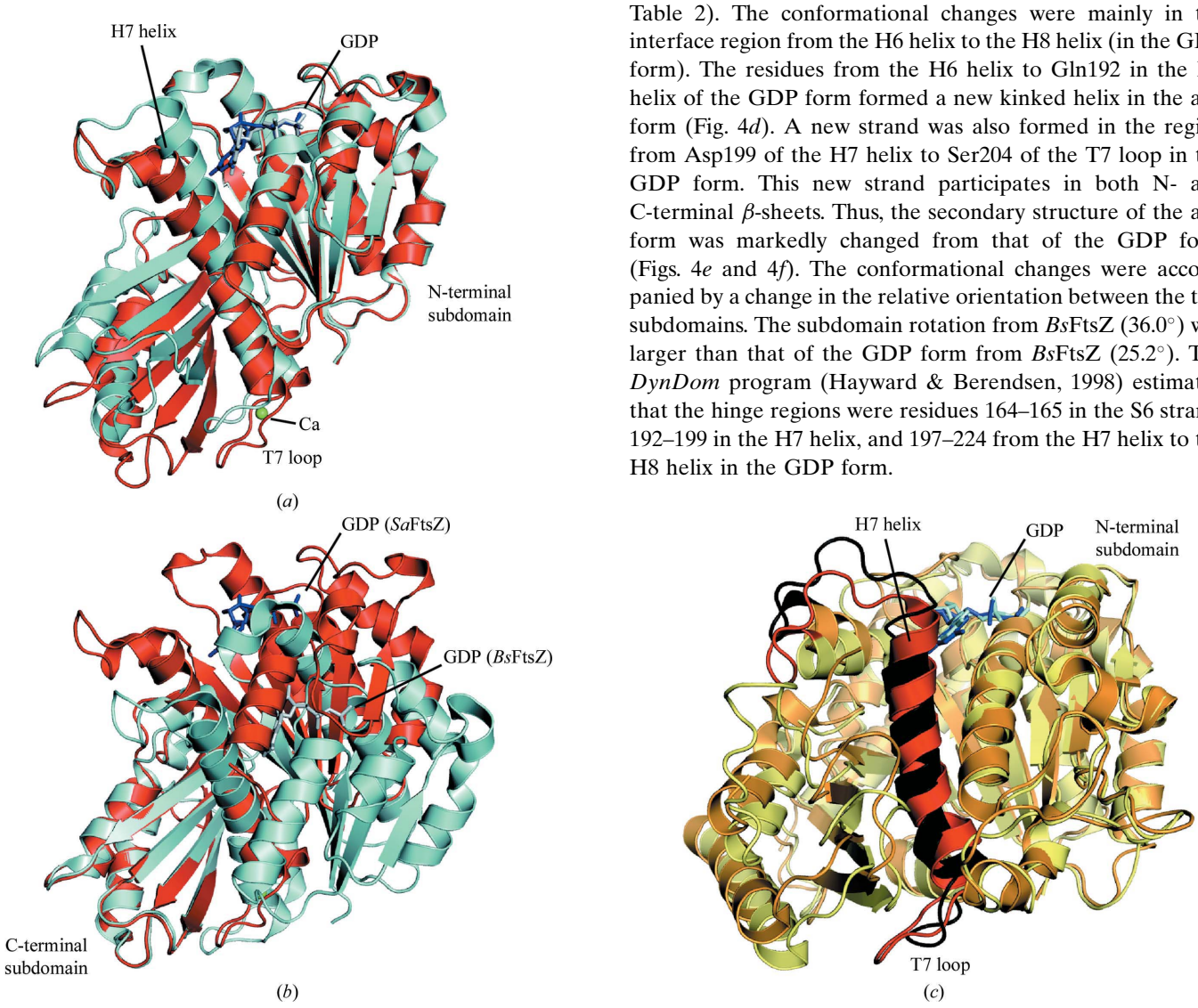

Figure 3
Structural comparisons (*a*, *b*) between GDP-form *Sa*FtsZ and GDP-form *Bs*FtsZ (PDB entry 2rhl) and (*c*) between straight (PDB entry 1jff; taxol complex; Löwe *et al.*, 2001) and curved (PDB entry 1sa0; colchicine complex; Ravelli *et al.*, 2004) β-tubulin. The structures in (*a*) and (*b*) are shown after superposition of the N-terminal subdomain (residues 13–171) and the C-terminal subdomain (residues 223–310), respectively. GDP-form *Sa*FtsZ and GDP-form *Bs*FtsZ are coloured red and cyan, respectively. GDPs bound to *Sa*FtsZ and *Bs*FtsZ are coloured blue and grey, respectively. In (*c*), straight and curved tubulin is shown in orange and yellow, respectively, after superposition of the N-terminal domain (residues 2–215). GDPs bound to the straight and the curved forms are represented as blue and cyan sticks, respectively. Subdomain-interface regions between the H6 helix and the T7 loop, including the H7 helix, in straight and curved tubulin are highlighted in red and black, respectively.

Conformational changes also occurred around the nucleotide-binding pocket in the N-terminal subdomain. The H7 helix moved away from the pocket and the T4 loop moved into and buried the pocket (Fig. 6). Although Phe183 in the H7 helix and Glu139 in the T5 loop showed significant interactions with nucleotides in the GDP form, these residues were no longer located near the pocket in the apo form. In particular, Phe183 in the H7 helix of the GDP form moved away by about 24 Å owing to the formation of the kinked helix in the apo form. All of these changes disrupted the nucleotide-binding pocket. In contrast, the conformation of the C-terminal subdomain was similar to that in the GDP form (Table 2, Supplementary Fig. S3*c*).

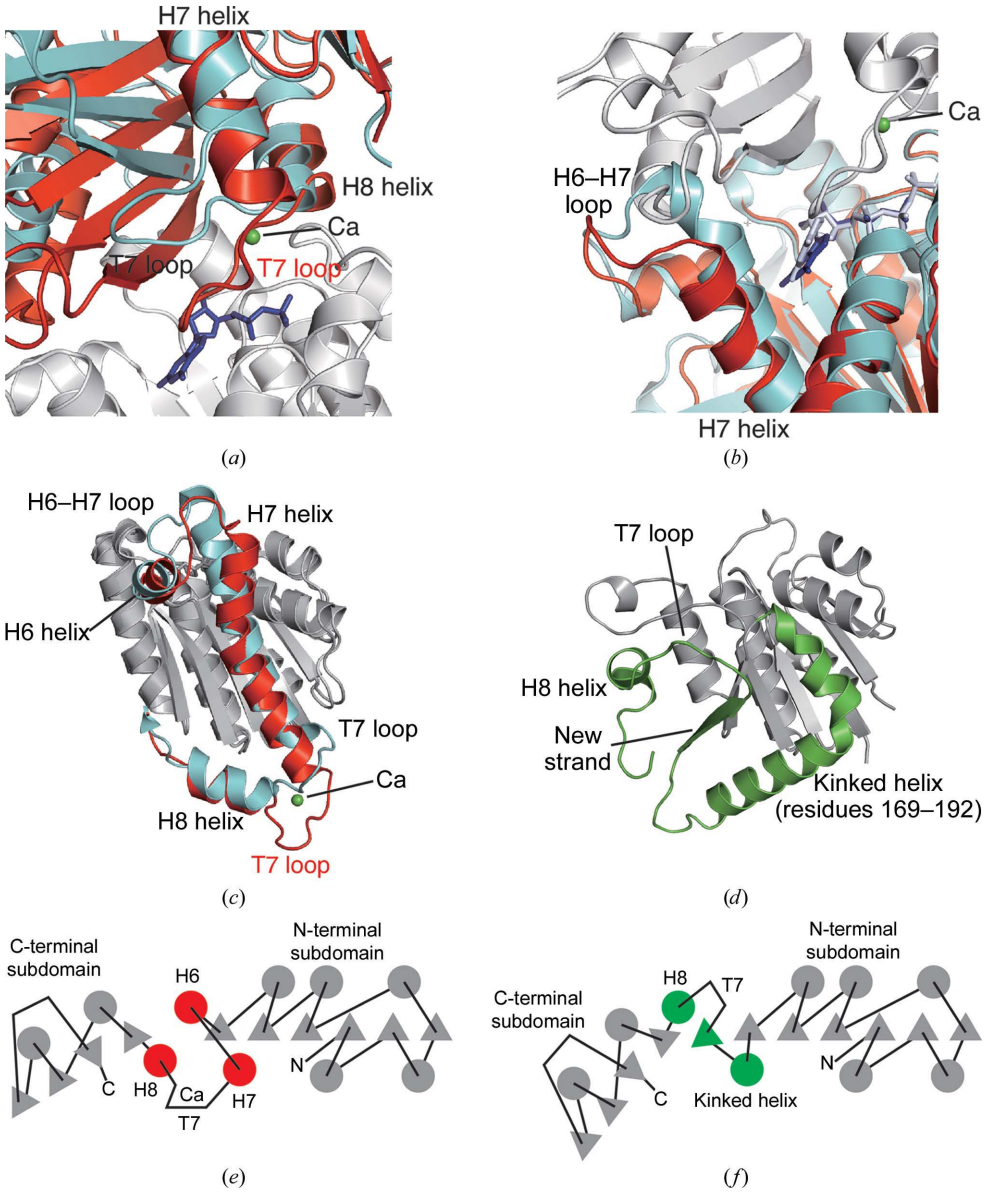

Figure 4
Structural changes in GDP-form and apo-form *Sa*FtsZ compared with canonical FtsZ structures. (*a*, *b*) Molecular structure and polymer association are compared between GDP-form *Sa*FtsZ (red) and the tilted dimer of *Mj*FtsZ (PDB entry 1w5a; cyan). (*a*) Interactions between the T7 loop and the 'lower' subunit (grey) are shown. The N-terminal subdomain (residues 13–171) of the GDP form in the lower subunit was superposed on the same region of the lower subunit of *Mj*FtsZ. GDP of *Sa*FtsZ and the calcium ion are represented as blue sticks and a green sphere, respectively. (*b*) Conformational differences around the H6–H7 loop are shown. This figure is superposed in the same manner as in (*a*). The 'upper' subunit of *Sa*FtsZ is shown in grey. GDP bound to *Sa*FtsZ and GTP bound to *Mj*FtsZ are shown as blue and sky-blue sticks, respectively. (*c*) Comparison of the interface region (from H6 helix to H8 helix) of the N- and C-terminal subdomains between GDP-form *Sa*FtsZ (red) and *Mj*FtsZ (cyan) showing that the H7 helix and T7 loop of *Sa*FtsZ are downshifted by about one helical pitch. The view is looking down from the C-terminal subdomain (residues 223–316) towards the N-terminal subdomain (residues 12–166) after superposition of the N-terminal subdomains of *Sa*FtsZ and *Mj*FtsZ (the N-terminal extra helix is omitted). The N-terminal subdomains of both structures are coloured grey and the C-terminal subdomain is not shown for clarity. (*d*) The conformation of the apo form is shown in the same manner as in (*c*). The interface region (corresponding to the region from H6 helix to H8 helix of the GDP form) is coloured green. (*e*, *f*) Topological diagrams of secondary structure are shown for (*e*) the GDP form and (*f*) the apo form. Circles and triangles indicate α-helices and β-strands, respectively. The interface region between subdomains of the GDP form and the apo form are coloured red and green, respectively.

3.5. Structure of *Sa*FtsZt-GDP complexed with PC190723 (PC190723 complex)

It has been shown that PC190723 binds to FtsZ with GTP, thereby promoting the polymerization of FtsZ (Andreu *et al.*, 2010). This can be interpreted as indicating that FtsZ with GTP creates a new cleft between the subdomains owing to the orientational change between the GDP-bound and GTP-bound states (Chen & Erickson, 2011). These observations suggested that PC190723 only interacts with straight FtsZ. However, the docking model calculated previously was based on curved FtsZ (Haydon *et al.*, 2008). As our *Sa*FtsZ-GDP structure has the features of straight FtsZ, we attempted to determine the structure of the complex between *Sa*FtsZt-GDP and PC190723 (the PC190723 complex).

The PC190723 complex crystal was obtained by cocrystallization and the structure was solved at a resolution of 2.70 Å by the molecular-replacement method (Table 1, Fig. 7). The unit-cell parameters of the PC190723 complex were very similar to those of *Sa*FtsZt-GDP. Based on the well defined $F_o - F_c$ map, we

found the ligand in a novel hydrophobic cleft (Fig. 7*c*) near the T7 loop, referred to as the PC-site, the conformation of which was stabilized by an octahedrally coordinated calcium ion. PC190723 possesses two distinct chemical moieties, benzamide and thiazolopyridine, both of which seem to make key interactions with *Sa*FtsZ (Fig. 7*c*). The ether linkage between the two moieties seems to function as an adjusting spacer that properly places the two moieties in the PC-site. The benzamide moiety of PC190723 has two important functional groups: the amide group and fluoro groups at the 2- and 6-positions. The amide group interacted with the PC-site in two ways: (i) the carbonyl group was bound to the calcium ion (3.2 Å) and (ii) the primary amino group was hydrogen bonded to the carbonyl of the Asn263 (3.4 Å) side chain as well as to the main-chain carbonyl of Val207 (2.9 Å). To simultaneously achieve proper coordination of the calcium ion and construction of the hydrogen-bond network, the amide group was twisted out of the plane of the benzene ring. The fluoro groups were located in the internal space surrounded by hydrophobic residues. While the 2-fluoro group was located in a hydrophobic core generated by residues Leu209 (3.1 Å) and Leu200 (3.5 Å), the 6-fluoro group was in a core generated by residues Val203 (3.5 Å) and Leu297 (3.5 Å). The thiazolopyridine moiety of PC190723 was located in a hydrophobic cleft between the H7 helix and the C-terminal subdomain formed by amino-acid residues Gly193 (3.8 Å), Gly196 (2.9 Å), Ile197 (4.4 Å), Met226 (4.1 Å), Ile228 (4.1 Å), Thr309 (3.3 Å) and Ile311 (3.3 Å). The 5-chloro group of the thiazolopyridine moiety was found in the hydrophobic space surrounded by Gly193 (3.8 Å), Met226 (4.1 Å) and Ile228 (4.1 Å). To examine whether a conformational change occurred upon PC190723 binding, we superposed the *Sa*FtsZ structures with and without PC190723. The structural comparison revealed some changes in the side-chain conformations, especially for Leu200, Val203, Ile228 and Thr309. Moreover, the water-mediated hydrogen-bond network was reconstructed. In the structure without PC190723, the calcium ion was coordinated by Asn208 O^{δ}, three main-chain carbonyls (Leu200, Val203 and Leu209) and two water molecules. In the structure with PC190723, the benzamide moiety replaced the inner of the two coordinating water molecules.

Very recently, the structure of the PC190723 complex was determined by another group independently of our work (Tan *et al.*, 2012). Although their crystal was obtained by a soaking method and the unit-cell parameters were slightly different from ours, the binding site appeared to be very similar. They showed that this site corresponds to the predominant locations of mutations that confer resistance to PC190723.

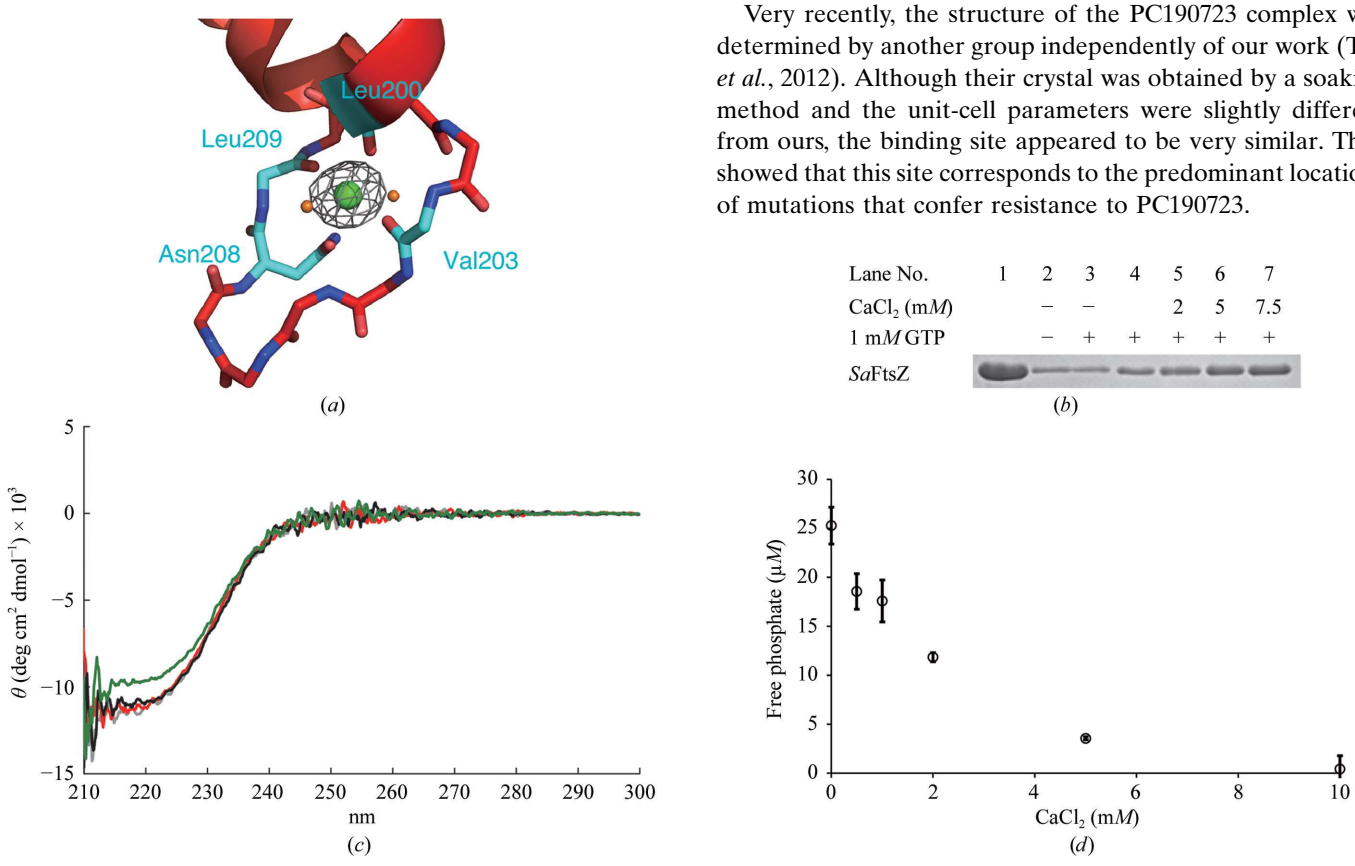

Figure 5
Interactions between the T7 loop and the calcium ion. (*a*) The residues of the T7 loop are indicated as sticks. The calcium ion was coordinated to Leu200, Val203, the side chain of Asn208 and Leu209. The calcium-bound residues are coloured cyan. The calcium ion and water molecules are represented as green and orange spheres, respectively. Grey mesh represents $F_o - F_c$ maps of the calcium ion displayed over 3.0σ. (*b*) Results of the sedimentation assay are shown. *Sa*FtsZf was incubated with 1 m*M* GTP in the presence of varying concentrations of $CaCl_2$. The samples in lanes 2–7 were precipitated by ultracentrifugation and the precipitates were then analyzed by SDS–PAGE. Lane 1, 15 µ*M* *Sa*FtsZf as a control; lane 2, precipitation without GTP and $CaCl_2$; lane 3, without $CaCl_2$; lane 4, 1 m*M* $CaCl_2$; lane 5, 2 m*M* $CaCl_2$; lane 6, 5 m*M* $CaCl_2$; lane 7, 7.5 m*M* $CaCl_2$; 1 m*M* GTP was added to the buffer in lanes 3–7. (*c*) CD spectra of *Sa*FtsZf with and without $CaCl_2$ are shown. 0.2 mg ml^{-1} *Sa*FtsZfs with or without 1 m*M* $CaCl_2$ was incubated at 298 K for 30 min in polymerization buffer with 1 m*M* GTP. Refolded *Sa*FtsZf with $CaCl_2$, refolded *Sa*FtsZf without $CaCl_2$, native *Sa*FtsZf with $CaCl_2$ and native *Sa*FtsZf without $CaCl_2$ are indicated by black, green, grey and red lines, respectively. (*d*) The GTPase activity of *Sa*FtsZf was inhibited by $CaCl_2$ in a concentration-dependent manner. The error bars represent the relevant standard deviations from three independent experiments.

4. Discussion

4.1. The conformation of the GDP form has the structural features of straight FtsZ

Previous investigations have suggested that FtsZ has a highly dynamic structure (Martín-Galiano *et al.*, 2010; Chen & Erickson, 2011; Mingorance *et al.*, 2001; Buey *et al.*, 2006). Based on the results of molecular-dynamics simulations, FtsZ has been suggested to have several distinct conformations with hinges around the H7 helix, and an assembly/disassembly cycle has been proposed which involves intermediate states including a GTP-bound curved polymer and a GDP-bound straight polymer (Martín-Galiano *et al.*, 2010). A large rotational change occurred between the subdomains on adding GTP to *Ec*FtsZ, probably resulting in the straight conformation (Chen & Erickson, 2011). However, all previously reported FtsZ structures were considered to have the curved conformation (Buey *et al.*, 2006; Oliva *et al.*, 2007), as exemplified by the tilted dimer of *Mj*FtsZ (Oliva *et al.*, 2004).

In this study, we found new conformations of FtsZ with and without bound nucleotide. The conformational changes from the previous structures occurred in the region from the H6 helix to the H8 helix and were accompanied by rearrangement of the inter-subdomain interactions. Although the bound nucleotide was GDP, the structure has the features of the straight conformation; the H6–H7 loop moved away from the

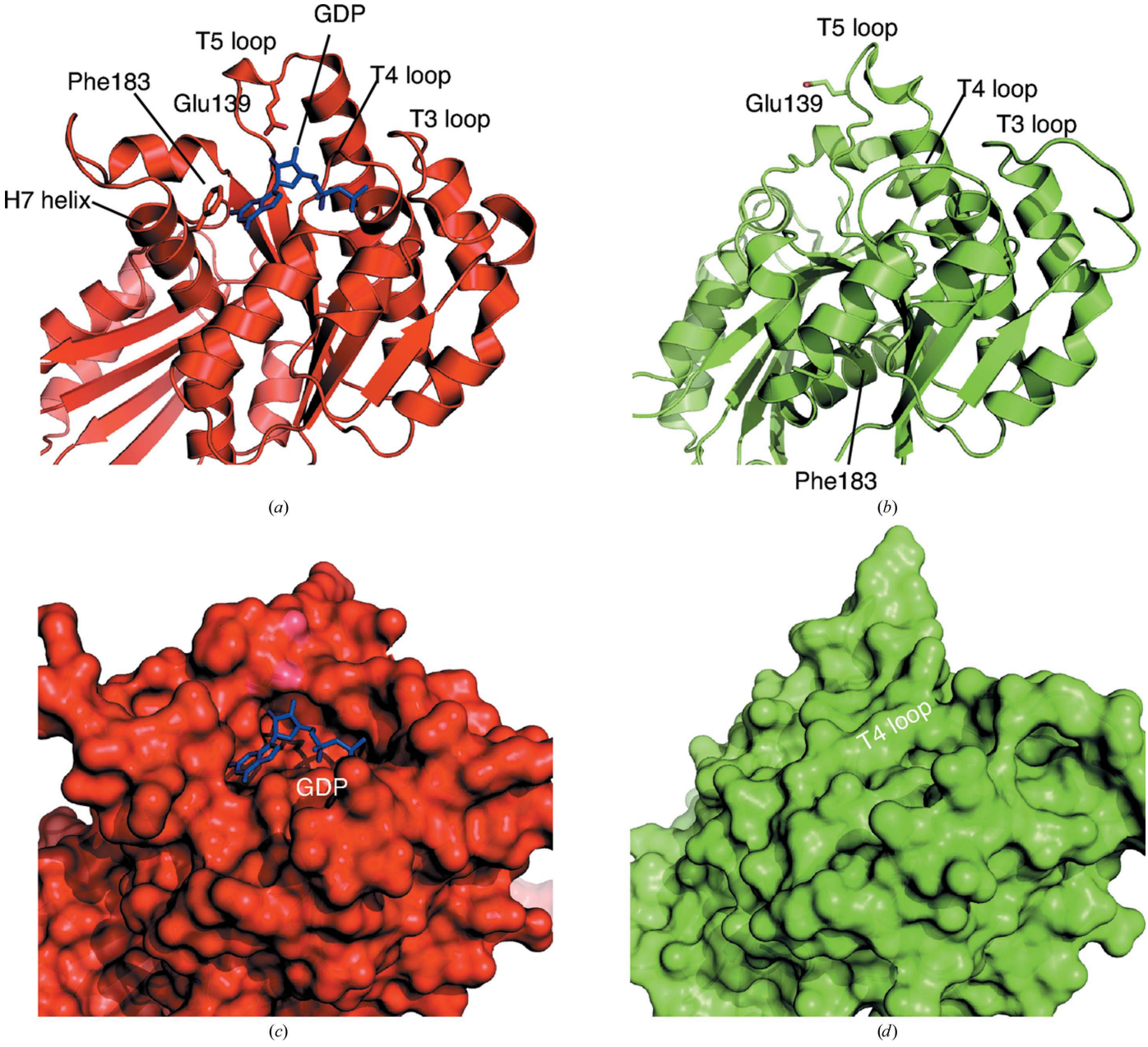

Figure 6
Structural comparison of the nucleotide-binding pockets of GDP-form (red) and apo-form (green) *Sa*FtsZ shown in cartoon (*a*, *b*) and surface (*c*, *d*) representations. GDP bound to the GDP form is represented as blue sticks. Note that the T4 loop overlaps the GDP site in the apo form.

nucleotide-binding pocket (Fig. 4*b*). The H7 helix was downshifted by one helical pitch (Fig. 4*c*) and the T7 loop was deeply inserted into the expanded pocket, placing the active residues close to the γ-phosphate and blocking solvent accessibility to the pocket (Fig. 4*a* and Supplementary Fig. S4). It should be noted that the eukaryotic homologue tubulin undergoes a similar structural change; the H7 helix in straight tubulin is downshifted in comparison with that in the curved conformation (Fig. 3*c*). All of these observations suggest that *Sa*FtsZ-GDP has the conformation of straight FtsZ just after

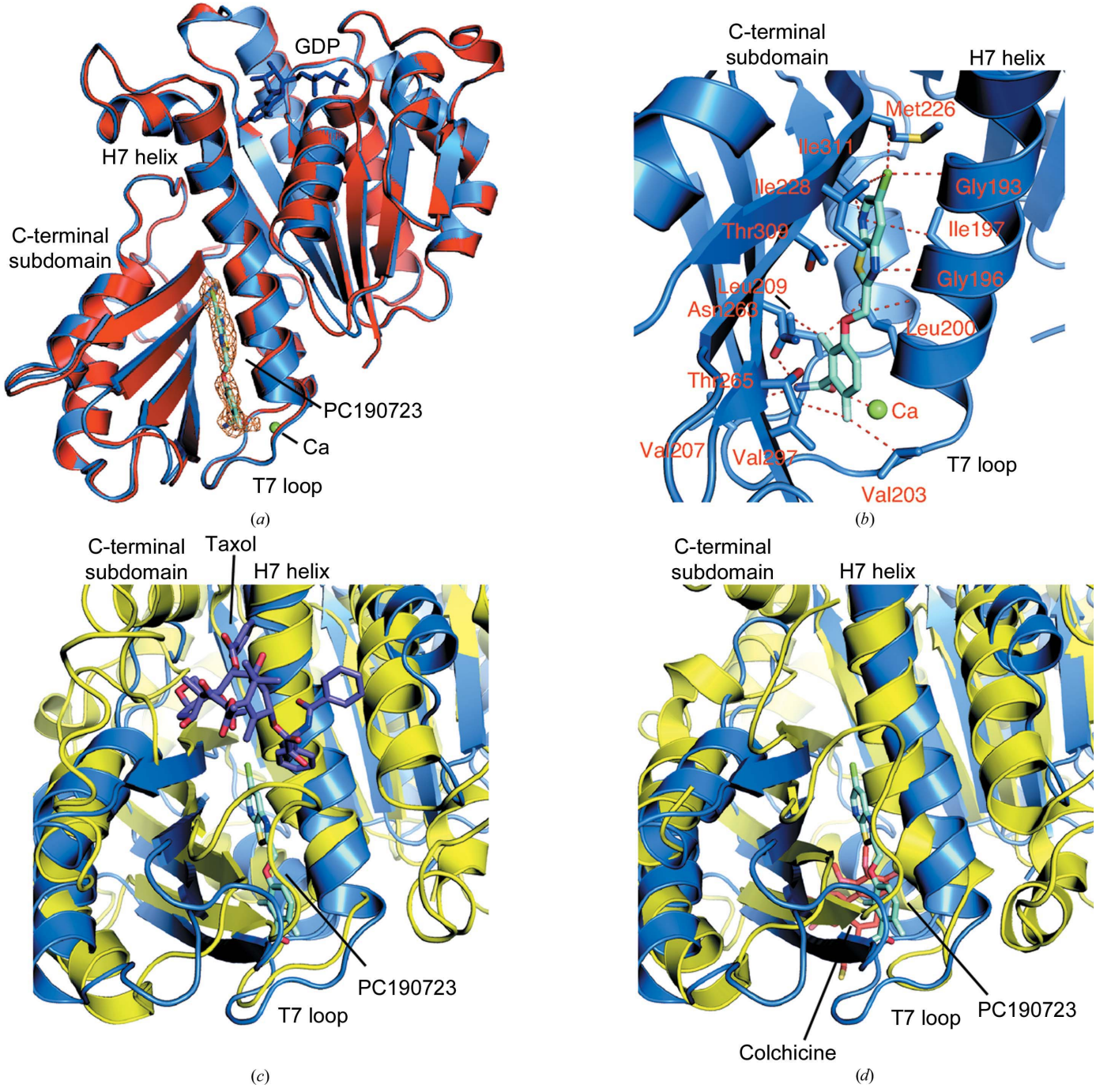

Figure 7
Crystal structure of the PC190723 complex. (*a*) Structure of the PC190723 complex (blue) superposed on that of the GDP form (red). GDP, a calcium ion and PC190723 in the PC190723 complex are represented as blue sticks, a green sphere and cyan sticks, respectively. Orange mesh represents the $F_o - F_c$ map of PC190723 displayed over 3.0σ. (*b*) Conformational detail of the PC-site. The residues interacting with PC190723 are indicated and their interactions are indicated by dotted lines. Cl, N, O, S, F and C atoms in PC190723 are coloured green, blue, red, yellow, sky-blue and cyan, respectively. (*c*) Structural comparison between the *Sa*FtsZ–PC190723 complex and the tubulin–taxol complex (PDB entry 1jff) after superposing the whole structures. Tubulin and taxol are represented as a yellow cartoon and magenta sticks, respectively. (*d*) Structural comparison between the *Sa*FtsZ–PC190723 complex and the tubulin–colchicine complex (PDB entry 1sa0) after superposing the whole structures. Tubulin and colchicine are represented as a yellow cartoon and red sticks, respectively.

GTP hydrolysis, as expected for the intermediate state of the GDP-bound straight polymer (Martín-Galiano *et al.*, 2010). The conformational change in tubulin is transmitted from one monomer to the other; thus, the intramolecular change may affect the intermolecular conformation (Ravelli *et al.*, 2004; Buey *et al.*, 2006). Similarly, the reorganization of the FtsZ subdomains may be an important factor affecting filament formation.

4.2. Molecular basis of the polymerization of FtsZs and the GTPase activity

We showed that the presence of calcium ions promoted the polymerization of *Sa*FtsZ and inhibited the GTPase activity (Fig. 5). However, it was unclear how calcium ions contributed to polymerization and inhibition at the molecular level. To determine the effect of calcium ions, we prepared a mutant in which Asn208 (an important residue for calcium coordination; Fig. 5*a*) was substituted by Ala. This mutant did not polymerize in the presence of calcium ions (Fig. 8*a*) and showed no GTPase activity (Fig. 8*b*).

GTPase activity is known to depend on FtsZ polymerization (Oliva *et al.*, 2004; Scheffers *et al.*, 2002). Asn208, Asp210 and Asp213 have been shown to be important for GTPase activity in *Ec*FtsZ (Scheffers *et al.*, 2002) and it was proposed that two aspartic acid residues in the upper subunit of *Mj*FtsZ polarize the attacking water molecule (Oliva *et al.*, 2004). However, the molecular details underlying this process are not known in the absence of the structure of GTP-bound straight FtsZ.

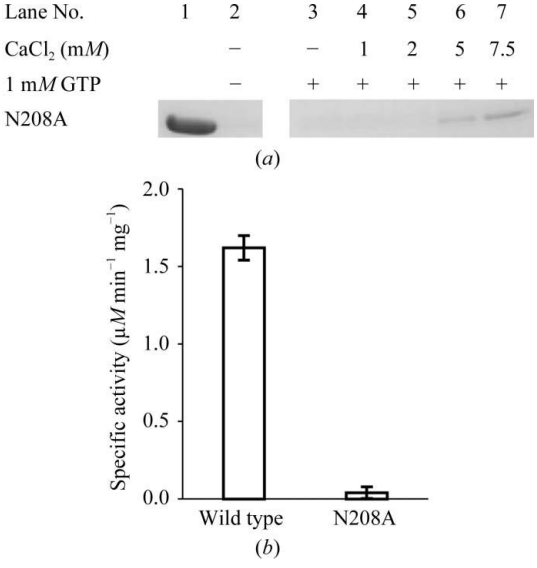

Figure 8
Sedimentation assay and GTPase activity of *Sa*FtsZf N208A. (*a*) 15 μ*M* *Sa*FtsZf N208A was incubated with 1 m*M* GTP in the presence of varying concentrations of $CaCl_2$. The samples in lanes 2–7 were precipitated by ultracentrifugation and the precipitates were analyzed by SDS–PAGE. Lane 1, 15 μ*M* *Sa*FtsZf N208A as a control; lane 2, precipitation without GTP and $CaCl_2$; lane 3, without $CaCl_2$; lane 4, 1 m*M* $CaCl_2$; lane 5, 2 m*M* $CaCl_2$; lane 6, 5 m*M* $CaCl_2$; lane 7, 7.5 m*M* $CaCl_2$; 1 m*M* GTP was added to the buffer in lanes 3–7. (*b*) GTPase specific activities of *Sa*FtsZf and *Sa*FtsZf N208A.

Structural comparison between *Sa*FtsZ-GDP and GTP-bound *Mj*FtsZ (Fig. 4*b*) suggested that the nucleotide-binding sites superposed well. Thus, we attempted to build a hypothetical GTP-bound straight model by adding a γ-phosphate to the *Sa*FtsZf structure (Fig. 9*a*). We built such a model without any steric hindrance and the model showed that Asp210 and Asp213 could bind to the γ-phosphate through water molecules (Figs. 9*a* and 9*c*). In contrast, Asn208 in the T7 loop could not interact with GTP. It is likely that Asn208 helps the calcium ion bind to the T7 loop, thereby forming the appropriate conformation for the T7 loop to be inserted into the nucleotide-binding pocket of the second molecule. Moreover, our structure suggested that the nucleotide is buried in the pocket by conformational change of the T7 loop. Thus, calcium ions promote the formation of a stable polymer owing to the slow hydrolysis to GDP. It is also possible that this conformational change makes it difficult to release the phosphate from the pocket.

4.3. Structure of the apo form

The apo-form structures determined previously were very similar to those of the previous GDP form (Oliva *et al.*, 2007), possibly because citrate or sulfate ions were located in the nucleotide-binding pocket. Unlike these previous observations, the conformation of the apo form found in the present study was very different from those in other FtsZs (Fig. 1). The nucleotide-binding pocket of the apo form was severely disrupted owing to conformational changes in the T4 loop, T5 loop and H7 helix (Figs. 6*b* and 6*d*). A similar conformational change in the T4 loop was also found in *M. tuberculosis* FtsZ, which did not bind the nucleotide (PDB entries 2q1x and 1rq2; Leung *et al.*, 2004). In the apo form, a new β-strand was formed at the H7 helix in the GDP form owing to calcium-ion chelation. This change could also occur in solution, as shown by CD measurements with and without calcium ions (Fig. 5*c*). The helical contents of *Sa*FtsZf with and without calcium ions were 34.9 and 32.0%, respectively, as calculated from the CD spectra. These values were consistent with those calculated from the obtained structures, *i.e.* 36.7 and 33.8%, respectively, assuming that the region from residue 317 to 390 does not adopt a helical conformation.

It has not been clarified at the molecular level how GDP is replaced by GTP. *Sa*FtsZ has several hinges around the H7 helix and has sufficient flexibility to act as a molecular switch in the assembly cycle. The present apo-form conformation may be one of the intermediate conformations in the physiological assembly cycle. It is possible that nucleotide turnover is caused not only by the difference in affinity between GTP and GDP but also by conformational change in the nucleotide-binding pocket.

4.4. Relative orientations between subdomains regulate the function of FtsZ

In the present study, we determined the structures of the apo form and GDP form of FtsZ by X-ray crystallography and found that FtsZ undergoes large conformational changes at

the subdomain interface. In particular, coordination of the calcium ion to the T7 loop contributed to this large change, regulating the polymerization and inhibition of GTPase activity (Fig. 5). However, we could not obtain crystals of the curved structure. It is possible that both structures are present under physiological conditions but that only the straight conformation of *Sa*FtsZ could be crystallized. It is also possible that the stable conformations of *Sa*FtsZ and other FtsZs differ and that a more stable straight conformation is obtained for *Sa*FtsZ.

It has been shown that PC190723 binds exclusively to the GTP form of FtsZ, thereby accelerating its polymerization (Andreu *et al.*, 2010). Therefore, it was speculated that FtsZ with GTP may form a new cleft between the subdomains owing to the reorientation between the GDP-bound and the GTP-bound states (Chen & Erickson, 2011). It has also been speculated that the binding site for PC190723 is similar to the taxol-binding site of tubulin (Haydon *et al.*, 2008). Taxol and PC190723 both stabilize straight polymers and both ligands were expected to target structurally related assembly switches (Andreu *et al.*, 2010; Elie-Caille *et al.*, 2007). In this study, we determined the structure of the PC190723 complex and found that PC190723 binds to the cleft (Fig. 7) located between the H7 helix and the C-terminal subdomain in close proximity to the T7 loop. This site does not necessarily correspond to the taxol-binding or colchicine-binding site of tubulin (Figs. 7*d* and 7*e*). However, the general inhibitory mechanism would be shared between the taxol and PC190723 cases. Alteration of the inter-subdomain orientations has been confirmed to be important for GTPase activity in FtsZ (Chen & Erickson, 2011). Binding of the ligand to the cleft fixes the movement and may prevent the active residues in the T7 loop from being located at the appropriate site for GTPase activity.

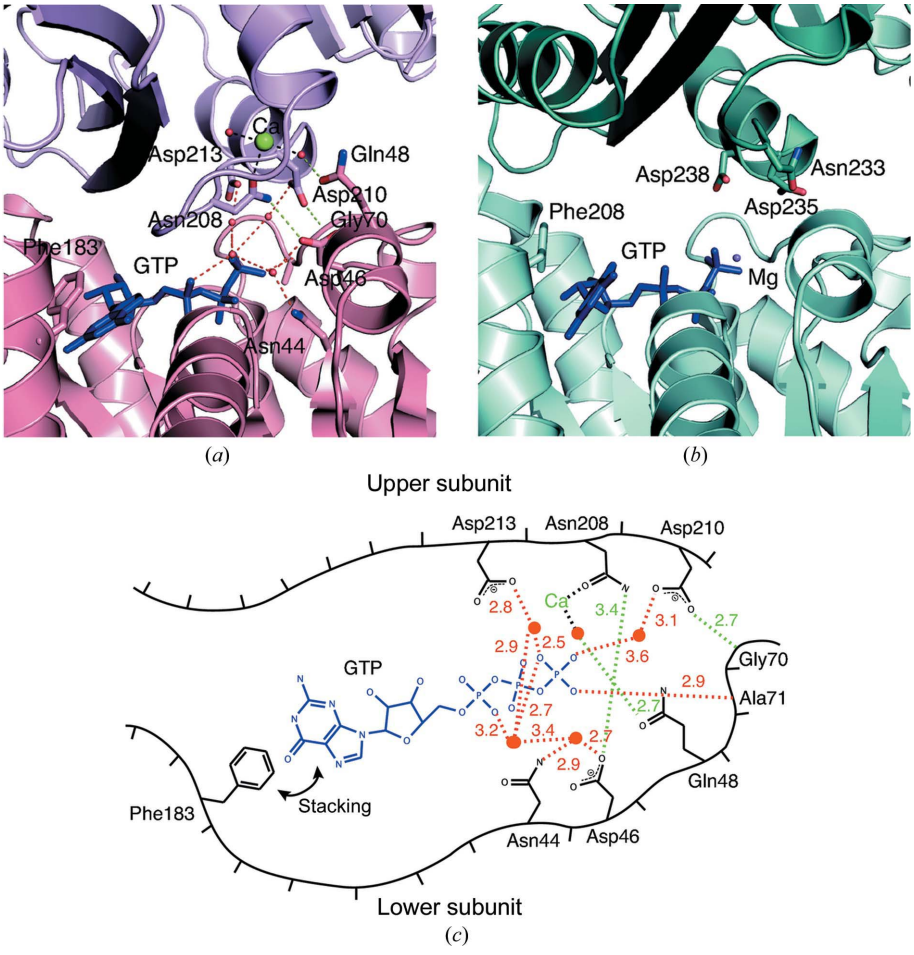

Figure 9
Hypothetical structural model of GTP-bound *Sa*FtsZ and its putative interactions. (*a*) The hypothetical GTP-bound model of *Sa*FtsZ is shown. This model was built based on superposition of *Sa*FtsZ-GDP and GTP-bound *Mj*FtsZ (see §2.4 and Fig. 4*b*). The upper and lower subunits of *Sa*FtsZ are coloured pink and salmon pink, respectively. GTP is coloured blue. The side chains of Asn208, Asp210 and Asp213 in the upper subunit and the side chains of Asn44, Asp46, Gln48 and Phe183 in the lower subunit are represented as sticks. Amide and carbonyl atoms in the side chains are coloured blue and red, respectively. The calcium ion and water molecules are represented as green and orange spheres, respectively. Hydrogen bonds between subunits are indicated by green dotted lines. Hydrogen bonds related to GTP are indicated by red dotted lines. Calcium coordinations are indicated by black dotted lines. (*b*) The tilted dimer interaction of GTP-bound *Mj*FtsZ (PDB entry 1w5a) is shown. *Mj*FtsZ was superposed on the N-terminal region (residues 13–171 in *Sa*FtsZ) of the lower subunit in (*a*). The illustrations are represented in the same manner as in (*a*). The upper and lower subunits of *Mj*FtsZ are coloured teal and cyan, respectively. GTP is coloured blue. The side chains of Phe208, Asp233, Asp235 and Asp238 are represented as sticks. Phe208, Asn233, Asp235 and Asp238 correspond to Phe183, Asn208, Asp210 and Asp213 in *Sa*FtsZ, respectively. The magnesium ion is represented as a magenta sphere. (*c*) The hydrogen-bond network around the phosphates of GTP in the hypothetical model is illustrated. Water molecules are represented as orange spheres. Hydrogen bonds are represented in the same manner as in (*a*). GTP is shown in blue. The distances (Å) of each hydrogen bond are indicated in the figure.

We thank the beamline scientists at SPring-8 and the Photon Factory for their help in collecting X-ray diffraction data. The synthesis and preparation of the PC190723 used in this study were arranged by Dr Ken-ichi Matsumura at Shionogi Co. Ltd. This work was supported in part by the Project for Developing Innovation Systems of the Ministry of Education, Culture, Sports, Science and Technology, Japan.

References

Adams, P. D. *et al.* (2010). *Acta Cryst.* D**66**, 213–221.
Adams, D. W. & Errington, J. (2009). *Nature Rev. Microbiol.* **7**, 642–653.
Andreu, J. M., Schaffner-Barbero, C., Huecas, S., Alonso, D., Lopez-Rodriguez, M. L., Ruiz-Avila, L. B., Núñez-Ramírez,

R., Llorca, O. & Martín-Galiano, A. J. (2010). *J. Biol. Chem.* **285**, 14239–14246.
Boer, P. de, Crossley, R. & Rothfield, L. (1992). *Nature (London)*, **359**, 254–256.
Brünger, A. T., Adams, P. D., Clore, G. M., DeLano, W. L., Gros, P., Grosse-Kunstleve, R. W., Jiang, J.-S., Kuszewski, J., Nilges, M., Pannu, N. S., Read, R. J., Rice, L. M., Simonson, T. & Warren, G. L. (1998). *Acta Cryst.* D**54**, 905–921.
Buey, R. M., Díaz, J. F. & Andreu, J. M. (2006). *Biochemistry*, **45**, 5933–5938.
Chang, C.-F., Shuman, H. & Somlyo, A. P. (1986). *J. Bacteriol.* **167**, 935–939.
Chen, Y. & Erickson, H. P. (2011). *Biochemistry*, **50**, 4675–4684.
DeLano, W. L. (2002). *PyMOL*. http://www.pymol.org.
Domadia, P., Swarup, S., Bhunia, A., Sivaraman, J. & Dasgupta, D. (2007). *Biochem. Pharmacol.* **74**, 831–840.
Elie-Caille, C., Severin, F., Helenius, J., Howard, J., Muller, D. J. & Hyman, A. A. (2007). *Curr. Biol.* **17**, 1765–1770.
Emsley, P. & Cowtan, K. (2004). *Acta Cryst.* D**60**, 2126–2132.
Harding, M. M. (1999). *Acta Cryst.* D**55**, 1432–1443.
Harding, M. M. (2001). *Acta Cryst.* D**57**, 401–411.
Haydon, D. J. *et al.* (2008). *Science*, **321**, 1673–1675.
Hayward, S. & Berendsen, H. J. (1998). *Proteins*, **30**, 144–154.
Holland, I. B., Jones, H. E., Campbell, A. K. & Jacq, A. (1999). *Biochimie*, **81**, 901–907.
Huecas, S. & Andreu, J. M. (2003). *J. Biol. Chem.* **278**, 46146–46154.
Jaiswal, R. & Panda, D. (2009). *J. Biochem.* **146**, 733–742.
Langer, G., Cohen, S. X., Lamzin, V. S. & Perrakis, A. (2008). *Nature Protoc.* **3**, 1171–1179.
Läppchen, T., Pinas, V. A., Hartog, A. F., Koomen, G. J., Schaffner-Barbero, C., Andreu, J. M., Trambaiolo, D., Löwe, J., Juhem, A., Popov, A. V. & den Blaauwen, T. (2008). *Chem. Biol.* **15**, 189–199.
Leung, A. K. W., White, E. L., Ross, L. J., Reynolds, R. C., DeVito, J. A. & Borhani, D. W. (2004). *J. Mol. Biol.* **342**, 953–970.
Lock, R. L. & Harry, E. J. (2008). *Nature Rev. Drug Discov.* **7**, 324–338.
Löwe, J. & Amos, L. A. (1998). *Nature (London)*, **391**, 203–206.
Löwe, J. & Amos, L. A. (1999). *EMBO J.* **18**, 2364–2371.
Löwe, J., Li, H., Downing, K. H. & Nogales, E. (2001). *J. Mol. Biol.* **313**, 1045–1057.
Lu, C., Reedy, M. & Erickson, H. P. (2000). *J. Bacteriol.* **182**, 164–170.
Margolin, W. (2005). *Nature Rev. Mol. Cell Biol.* **6**, 862–871.
Marrington, R., Small, E., Rodger, A., Dafforn, T. R. & Addinall, S. G. (2004). *J. Biol. Chem.* **279**, 48821–48829.
Martín-Galiano, A. J., Buey, R. M., Cabezas, M. & Andreu, J. M. (2010). *J. Biol. Chem.* **285**, 22554–22565.
Mingorance, J., Rueda, S., Gómez-Puertas, P., Valencia, A. & Vicente, M. (2001). *Mol. Microbiol.* **41**, 83–91.
Mosyak, L., Zhang, Y., Glasfeld, E., Haney, S., Stahl, M., Seehra, J. & Somers, W. S. (2000). *EMBO J.* **19**, 3179–3191.
Mukherjee, A. & Lutkenhaus, J. (1999). *J. Bacteriol.* **181**, 823–832.
Murshudov, G. N., Skubák, P., Lebedev, A. A., Pannu, N. S., Steiner, R. A., Nicholls, R. A., Winn, M. D., Long, F. & Vagin, A. A. (2011). *Acta Cryst.* D**67**, 355–367.
Ohashi, Y., Chijiiwa, Y., Suzuki, K., Takahashi, K., Nanamiya, H., Sato, T., Hosoya, Y., Ochi, K. & Kawamura, F. (1999). *J. Bacteriol.* **181**, 1348–1351.
Oliva, M. A., Cordell, S. C. & Löwe, J. (2004). *Nature Struct. Mol. Biol.* **11**, 1243–1250.
Oliva, M. A., Trambaiolo, D. & Löwe, J. (2007). *J. Mol. Biol.* **373**, 1229–1242.
Otwinowski, Z. & Minor, W. (1997). *Methods Enzymol.* **276**, 307–326.
Pichoff, S. & Lutkenhaus, J. (2002). *EMBO J.* **21**, 685–693.
Price, N. C. & Nairn, J. (2009). *Exploring Proteins: A Student's Guide to Experimental Skills and Methods*. Oxford University Press.
Ravelli, R. B., Gigant, B., Curmi, P. A., Jourdain, I., Lachkar, S., Sobel, A. & Knossow, M. (2004). *Nature (London)*, **428**, 198–202.
RayChaudhuri, D. & Park, J. T. (1992). *Nature (London)*, **359**, 251–254.
Raymond, A., Lovell, S., Lorimer, D., Walchli, J., Mixon, M., Wallace, E., Thompkins, K., Archer, K., Burgin, A. & Stewart, L. (2009). *BMC Biotechnol.* **9**, 37.
Rice, L. M., Earnest, T. N. & Brunger, A. T. (2000). *Acta Cryst.* D**56**, 1413–1420.
Scheffers, D. J., de Wit, J. G., den Blaauwen, T. & Driessen, A. J. (2002). *Biochemistry*, **41**, 521–529.
Sheldrick, G. M. (2008). *Acta Cryst.* A**64**, 112–122.
Sheldrick, G. M. (2010). *Acta Cryst.* D**66**, 479–485.
Stokes, N. R. *et al.* (2005). *J. Biol. Chem.* **280**, 39709–39715.
Tan, C. M. *et al.* (2012). *Sci. Transl. Med.* **4**, 126ra35.
Terwilliger, T. C. (2000). *Acta Cryst.* D**56**, 965–972.
Vagin, A. & Teplyakov, A. (2010). *Acta Cryst.* D**66**, 22–25.
Winn, M. D. *et al.* (2011). *Acta Cryst.* D**67**, 235–242.
Yan, K., Pearce, K. H. & Payne, D. J. (2000). *Biochem. Biophys. Res. Commun.* **270**, 387–392.
Yao, M., Zhou, Y. & Tanaka, I. (2006). *Acta Cryst.* D**62**, 189–196.
Yu, X.-C. & Margolin, W. (1997). *EMBO J.* **16**, 5455–5463.
Zhou, Y., Yao, M. & Tanaka, I. (2006). *J. Appl. Cryst.* **39**, 57–63.